

μDamID: a microfluidic approach for imaging and sequencing protein-DNA interactions in single cells

Authors: Nicolas Altemose¹, Annie Maslan¹, Andre Lai¹, Jonathan A. White¹,
Aaron M. Streets^{1,2,*}

¹Department of Bioengineering, University of California, Berkeley, Berkeley, CA, 94720

²Chan Zuckerberg Biohub, San Francisco, CA 94158

* To whom correspondence should be addressed. Email: astreet@berkeley.edu

1 **Abstract**

2

3 Genome regulation depends on carefully programmed protein-DNA interactions that maintain or
4 alter gene expression states, often by influencing chromatin organization. Most studies of these
5 interactions to date have relied on bulk methods, which in many systems cannot capture the
6 dynamic single-cell nature of these interactions as they modulate cell states. One method allowing
7 for sensitive single-cell mapping of protein-DNA interactions is DNA adenine methyltransferase
8 identification (DamID), which records a protein's DNA-binding history by methylating adenine
9 bases in its vicinity, then selectively amplifies and sequences these methylated regions. These
10 interaction sites can also be visualized using fluorescent proteins that bind to methyladenines. Here
11 we combine these imaging and sequencing technologies in an integrated microfluidic platform
12 (μ DamID) that enables single-cell isolation, imaging, and sorting, followed by DamID. We apply
13 this system to generate paired single-cell imaging and sequencing data from a human cell line, in
14 which we map and validate interactions between DNA and nuclear lamina proteins, providing a
15 measure of 3D chromatin organization and broad gene regulation patterns. μ DamID provides the
16 unique ability to compare paired imaging and sequencing data for each cell and between cells,
17 enabling the joint analysis of the nuclear localization, sequence identity, and variability of protein-
18 DNA interactions.

19

20

21

22

23

24 **Introduction**

25 Complex life depends on the protein-DNA interactions that constitute and maintain the epigenome,
26 including interactions with histone proteins, transcription factors, DNA (de)methylases, and
27 chromatin remodeling complexes, among others. These interactions enable the static DNA
28 sequence inside the nucleus to dynamically execute different gene expression programs that shape
29 the cell's identity and behavior. Methods for measuring protein-DNA interactions have proven
30 indispensable for understanding the epigenome, though to date most of this knowledge has derived
31 from experiments in bulk cell populations. By requiring large numbers of cells, these bulk methods
32 can fail to capture critical epigenomic processes that occur in small numbers of dividing cells,
33 including processes that influence embryo development, developmental diseases, stem cell
34 differentiation, and certain cancers. By averaging together populations of cells, bulk methods also
35 fail to capture important epigenomic dynamics occurring in asynchronous single cells during
36 differentiation or the cell cycle. Because of this, bulk methods can overlook important biological
37 heterogeneity within a tissue. It also remains difficult to pair bulk biochemical data with imaging
38 data, which inherently provide information in single cells, and which can reveal the spatial location
39 of protein-DNA interactions within the nuclei of living cells. These limitations underline the need
40 for high-sensitivity single-cell methods for measuring protein-DNA interactions.

41

42 Most approaches for mapping protein-DNA interactions rely on immunoaffinity purification, in
43 which protein-DNA complexes are physically isolated using a high-affinity antibody against the
44 protein, then purified by washing and de-complexed so the interacting DNA can be amplified and
45 measured. The most widely used among these methods is chromatin immunoprecipitation with
46 sequencing (ChIP-seq; Barski et al. 2007, Johnson et al. 2007), which has formed the backbone of

47 several large epigenome mapping projects (Celniker et al. 2009; ENCODE Consortium 2012;
48 Kundaje et al. 2015). One drawback of ChIP-seq is that the protein-DNA complex, which is often
49 fragile, must survive the shearing or digestion of the surrounding DNA, as well as several
50 intermediate washing and purification steps, in order to be amplified and sequenced. This results
51 in a loss of sensitivity, especially when using a small amount of starting material. More recent
52 immunoaffinity-based methods have reduced the high input requirements of ChIP-seq, but they
53 recover relatively few interactions in small numbers of cells or single cells (Wu et al. 2012, Shen
54 et al. 2014, Jakobsen et al. 2015, Rotem et al. 2015, Zhang et al. 2016, Skene et al. 2018, Harada
55 et al. 2018, Kaya-Okur et al. 2019, Carter et al. 2019, Grosselin et al. 2019).

56
57 An alternative method for probing protein-DNA interactions, called DNA adenine
58 methyltransferase identification (DamID), relies not on physical separation of protein-DNA
59 complexes (as in ChIP-seq), but on a sort of ‘chemical recording’ of protein-DNA interactions
60 onto the DNA itself, which can later be selectively amplified (Figure 1a; van Steensel and Henikoff
61 2000, Vogel et al. 2007). This method utilizes a small enzyme from *E. coli* called DNA adenine
62 methyltransferase (Dam). When genetically fused to the protein of interest, Dam deposits methyl
63 groups near the protein-DNA contacts at the N6 positions of adenine bases (^{m6}A) within GATC
64 sequences (which occur once every 270 bp on average across the human genome). That is,
65 wherever the protein contacts DNA throughout the genome, ^{m6}A marks are left at GATC sites in
66 its trail. These ^{m6}A marks are highly stable in eukaryotic cells, which do not tend to methylate (or
67 demethylate) adenines (O’Brown et al. 2019). Dam expression has been shown to have no
68 discernable effect on gene expression in a human cell line, and its ^{m6}A marks were shown to be
69 passed to daughter cells, halving in quantity each generation after Dam is inactivated (Park et al.

70 2018). These properties allow even transient protein-DNA interactions to be recorded as
71 permanent, biologically orthogonal chemical signals on the DNA.

72

73 DamID reads out these chemical recordings of protein-DNA interactions by specifically
74 amplifying and then sequencing fragments of DNA containing the interaction site. First, genomic
75 DNA is purified and digested with DpnI, a restriction enzyme that exclusively cleaves G^{m6}ATC
76 sites (Figure 1). Then, universal adapters are ligated onto the fragment ends to allow for
77 amplification using universal primers. Only regions with a high density of m⁶A produce DNA
78 fragments short enough to be amplified by Polymerase Chain Reaction (PCR) and quantified by
79 microarray or high-throughput sequencing (Wu et al. 2016). DamID has been used to explore
80 dynamic regulatory protein-DNA interactions such as transcription factor binding (Orian et al.
81 2003) and RNA polymerase binding (Southall et al. 2013) as well as protein-DNA interactions
82 that maintain large-scale genome organization. One frequent application of DamID is to study
83 large DNA domains associated with proteins at the nuclear lamina, near the inner membrane of
84 the nuclear envelope (Pickersgill et al. 2006, Guelen et al. 2008, reviewed by van Steensel and
85 Belmont 2017). Because DamID avoids the limitations of antibody binding, physical separations,
86 or intermediate purification steps, it lends itself to single-cell applications. Recently, DamID has
87 been successfully applied to sequence lamina-associated domains (LADs) in single cells in a one-
88 pot reaction, recovering hundreds of thousands of unique fragments per cell (Kind et al. 2015).

89

90 While DamID maps the sequence positions of protein-DNA interactions throughout the genome,
91 the spatial location of these interactions in the nucleus can play an important role in genome
92 regulation (Bickmore and van Steensel 2013). A recent technique demonstrated the ability to

93 specifically label and visualize protein-DNA interactions using fluorescence microscopy,
94 revealing their spatial location within the nucleus in live cells (Kind et al. 2013). Visualization
95 requires co-expression of a different fusion protein called ^{m6}A-Tracer, which contains green
96 fluorescent protein (GFP) and a domain that binds specifically to methylated GATC sites. This
97 imaging technology has been applied to visualize the dynamics of LADs within single cells (Kind
98 et al. 2013). Many recent efforts have aimed to measure chromatin organization in single cells, to
99 better understand the heterogeneity of cells within tissues and the biological underpinnings of their
100 gene expression states (reviewed by Kelsey et al. 2017). Both imaging and sequencing protein-
101 DNA interactions can provide useful single-cell epigenomic information, but despite recent
102 advances in single-cell sequencing technologies, it remains fundamentally difficult to track
103 individual cells and pair their sequencing data with other measurements such as imaging. Pairing
104 imaging and sequencing data could be applied to study, for example, how the dynamic remodeling
105 of chromatin proteins across the genome in developing cells relates to the localization of those
106 proteins in the nucleus.

107

108 Here we aimed to pair DamID with ^{m6}A-Tracer imaging to produce coupled imaging and
109 sequencing measurements of protein-DNA interactions in the same single cells. To achieve this,
110 we engineered an integrated microfluidic device that enables single-cell isolation, imaging,
111 selection, and DamID processing, which we call “μDamID.” We applied our device to image and
112 map nuclear lamina interactions in a transiently transfected human cell line co-expressing ^{m6}A-
113 Tracer, and we validated our measurements against bulk DamID data from the same cell line as
114 well as other human cell lines (Lenain et al. 2017, Kind et al. 2015). We discuss the advantages
115 and potential applications of our device as well as future improvements to this system.

116 **Results and Discussion**

117 *Design and operation of a microfluidic device with valve-actuated active cell traps*

118 We designed and fabricated a polydimethylsiloxane (PDMS) microfluidic device with integrated
119 elastomeric valves to facilitate the various reaction stages of the DamID protocol in a single liquid
120 phase within the same device (Figure 1). The device is compatible with high-magnification imaging
121 on inverted microscopes, enabling imaging prior to cell lysis. Each device was designed to process
122 10 cells in parallel, each in an individual reaction lane fed from a common set of inlets. Valves are
123 controlled by pneumatic actuators operated electronically via a programmable computer interface
124 (White and Streets 2018).

125
126 Device operation was modified from our previous single-cell RNA sequencing platform (Streets
127 et al. 2014). A suspension of single cells is loaded into the cell inlet (Figure 1b) and cells are
128 directed towards a trapping region by a combination of pressure-driven flow and precise peristaltic
129 pumping. As a cell crosses one of the 10 trapping regions, valves are actuated to immobilize the
130 cell for imaging (Supplementary Figure 1). The cell is imaged by confocal fluorescence
131 microscopy to visualize the localization of ^{m6}A-Tracer, and after image acquisition, the user can
132 choose whether to select the cell for DamID processing, or to reject it and send it out the waste
133 outlet (Figure 1b).

134
135 Selected cells are injected from the trapping region into a holding chamber using pressure-driven
136 flow from the reagent inlet (Figure 1b, Supplementary Figure 1). Once all 10 holding chambers
137 are filled with imaged cells, processing proceeds in parallel for all 10 cells by successively adding
138 the necessary reagents for each step of the single-cell DamID protocol (Kind et al. 2015) and dead-

139 end filling each of the subsequent reaction chambers. Reaction temperatures are controlled by
140 placing the device on a custom-built thermoelectric control unit for dynamic thermal cycling.
141 Enzymes are heat inactivated between each step (Kind et al. 2015) and a low concentration of mild
142 detergent was added to all reactions to prevent enzyme adhesion to PDMS (Streets et al. 2014).

143

144 Figure 1 shows a schematic of the microfluidic processing work flow. In the first reaction stage, a
145 buffer containing detergent and proteinase pushes the cell into the lysis chamber, where its
146 membranes are lysed and its proteins, including ^{m6}A-Tracer, are digested away. Next, a DpnI
147 reaction mix is added to digest the genomic DNA at Dam-methylated GATC sites in the digestion
148 chamber. Then, a mix of DamID universal adapter oligonucleotides and DNA ligase is added to
149 the ligation chamber. Finally, a PCR mix is added containing primers that anneal to the universal
150 adapters is added and all valves within the lane are opened, creating a 120 nl cyclic reaction
151 chamber. Contents are thoroughly mixed by peristaltic pumping around the reaction ring, then
152 PCR is carried out on-chip by thermocycling. Amplified DNA is collected from each individual
153 lane outlet, and sequencing library preparation is carried out off-chip.

154

155 *Application to map lamina-associated domains in a human cell line*

156 We evaluated the performance of this platform by mapping the sequence and spatial location of
157 lamina-associated domains in a human cell line, allowing us to compare our data to previously
158 published LAD maps from DamID experiments in human cell lines (Kind et al. 2015, Lenain et
159 al. 2017). LADs are large (median 500 kb) and comprise up to 30% of the genome in human cells
160 (Guelen et al. 2008). LADs serve both a structural function, acting as a scaffold that underpins the
161 three-dimensional architecture of the genome in the nucleus, and a regulatory function, as LADs

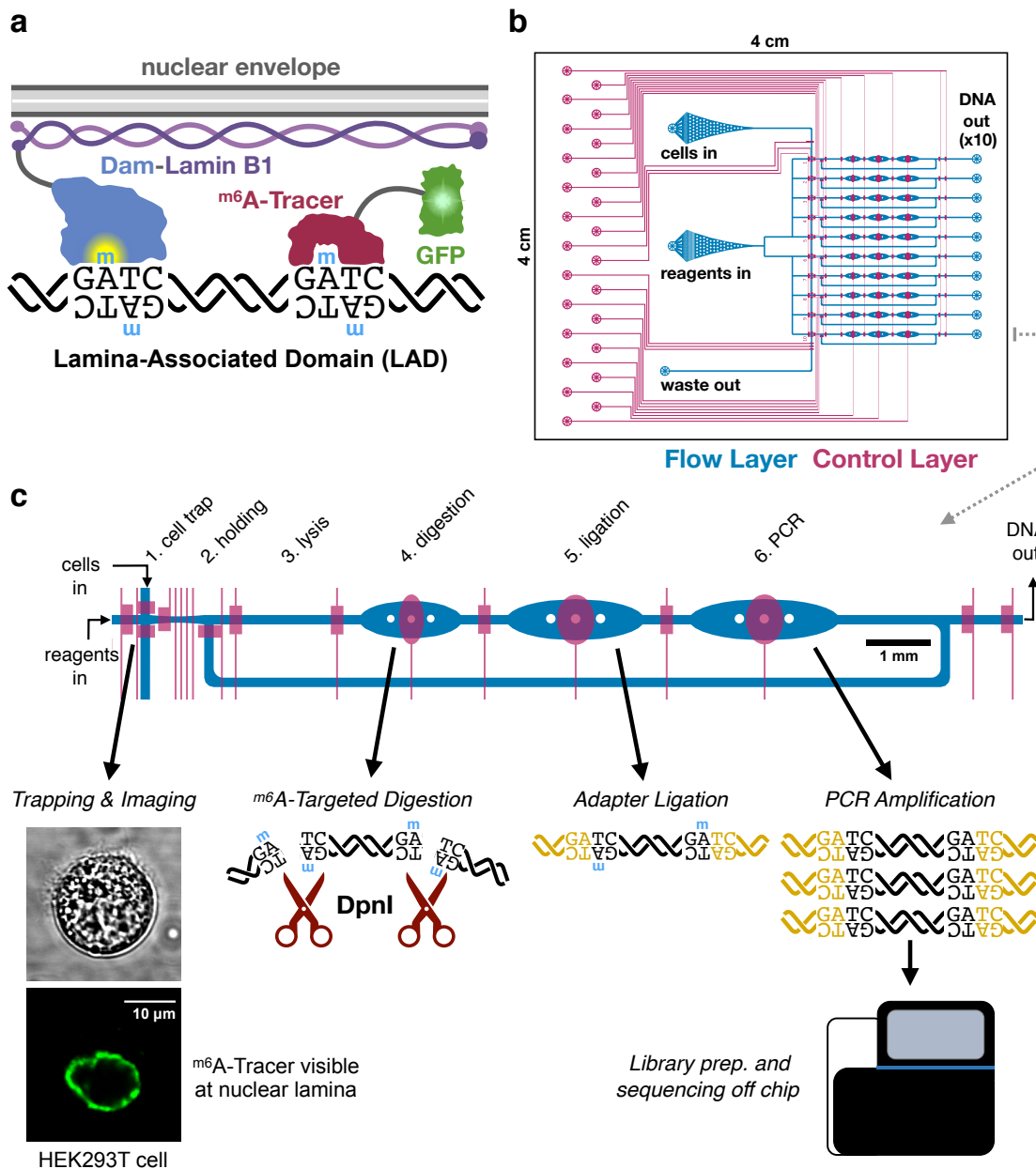


Figure 1. μ DamID device design and function. **a)** overview of DamID (van Steensel and Henikoff 2000) and m^6A -Tracer (Kind et al. 2013) technologies applied to study interactions between DNA and nuclear lamina proteins. **b)** the overall design of the 10-cell device, showing the flow layer (blue, where cells and reagents enter channels) and the control layer (red, where elastomeric valves overlap the flow layer to control the flow of liquids). **c)** a closer view of one lane explaining the DamID protocol and the function of each chamber of the device. 10 cells are trapped, imaged, and selected serially, one per lane, then all 10 cells are lysed and processed in parallel.

184 tend to be gene-poor, more heterochromatic, and transcriptionally less active (reviewed by van
185 Steensel and Belmont 2017 and Buchwalter et al. 2018). ^{m6}A-Tracer has previously been applied
186 to visualize LADs, which appear as a characteristic ring around the nuclear periphery in confocal
187 fluorescence microscopy images (Kind et al. 2013; Figure 1c).

188

189 We carried out experiments in HEK293T cells for their ease of growth, transfection, suspension,
190 and isolation. To enable rapid expression of Dam and ^{m6}A-Tracer transgenes, we transiently
191 transfected cells with DNA plasmids containing genes for a drug-inducible Dam-LMN1 fusion
192 protein as well as constitutively expressed ^{m6}A-Tracer. We then induced Dam-LMN1 expression,
193 optimizing the expression times to maximize the proportion of cells with fluorescent laminar rings
194 (Figure 1c). Because transient transfection yields a heterogeneous population of cells, each with
195 potentially variable copies of the transgenes, it was important for us to be able to image cells and
196 select only those with visible laminar rings, which were more likely to have the correct expression
197 levels, and which were unlikely to be in the mitosis phase of the cell cycle. This kind of complex
198 sorting would not be possible with sorting methods like fluorescence-activated cell sorting (FACS)
199 but is straight-forward in our microfluidic platform.

200

201 In addition to processing Dam-LMN1 cells, we transfected cells with the Dam gene alone, not
202 fused to LMN1, to provide a negative control demonstrating where the unfused Dam enzyme
203 would mark the genome if not tethered to the nuclear lamina (Vogel et al. 2007). This control is
204 useful for estimating the background propensity for each genomic region to be methylated, since
205 Dam preferentially methylates more accessible regions of the genome, including gene-rich regions
206 (Singh and Klar 1992, Lenain et al. 2017, Aughey et al. 2018). We selected Dam-only cells that

207 had high fluorescence levels across the nucleus and did not appear mitotic. We also performed
208 DamID in bulk transiently transfected HEK293T cells for validation (Vogel et al. 2007). We used
209 a mutant of Dam (V133A; Elsayy and Chahar 2014), which is predicted to have weaker
210 methylation activity than the wild-type allele on unmethylated DNA, to reduce background
211 methylation. We performed bulk DamID experiments comparing the mutant and wild-type alleles
212 and found that the V133A mutant allele provides more than twofold greater signal-to-background
213 compared to the wild-type allele (Supplementary Figure 2). We also performed RNA sequencing
214 in bulk cells that were untreated or transfected with Dam-only, Dam-LMNB1, or ^{m6}A-Tracer, and
215 we found only two differentially expressed genes (Supplementary Figure 3). This corroborates
216 similar published findings by others showing that Dam expression and adenine methylation have
217 little or no effect on gene expression in HEK293T cells (Park et al. 2018).

218

219 We ran three devices containing 25 imaged cells total, with empty lanes left as negative controls,
220 which did not yield sequenceable quantities of DNA. From these, we selected 18 cells total for
221 multiplexed sequencing, including 15 Dam-LMNB1 cells and 3 Dam-only cells, to achieve a
222 desired level of coverage per cell. Selection was based on image quality and initial DNA
223 quantification data from each sample (see Methods). We included one anomalous Dam-LMNB1
224 cell that appeared to have high fluorescence in the nuclear interior, predicting that it might have
225 higher background DamID coverage in non-LAD regions (cell #7). After sequencing, we excluded
226 3 Dam-LMNB1 cells containing a high fraction of sequencing reads mapping to the transfected
227 plasmids (Supplementary Figure 4); the 15 remaining cells had less than 5% of mapped reads
228 mapping to plasmid DNA. For these 15 remaining cells, we obtained a median of roughly 600,000

229 raw reads per cell (range 300k– 2.7M), covering a median of 110,000 unique DpnI fragments per
230 cell (37k – 370k), in line with previous DamID results from single cells (Kind et al. 2015).

231

232 *μDamID sequencing data recapitulate existing LAD maps*

233 To assess whether our single-cell μ DamID sequencing data provide accurate measurements of
234 lamina-associated domains, we first compared our single-cell results to those we obtained from
235 bulk DamID in the same cell line. DamID results are reported as a difference or log ratio between
236 the observed coverage from Dam-LMNB1 expressing cells and the expected coverage from
237 background, estimated using coverage from Dam-only expressing cells (see Methods). This
238 measure is reported within fixed 250 kb bins across the genome, which is half the median length
239 of known LADs in the genome (Kind et al. 2015). By aggregating the data from 11 Dam-LMNB1
240 expressing cells passing filters and excluding the anomalous cell #7, we found excellent
241 correspondence with the bulk data obtained from millions of cells (Figure 2a), with a Pearson
242 correlation of 0.85 across all bins in the genome. To ensure normalization is not inflating the
243 correlation, we compared aggregate single-cell raw read coverage to bulk raw read coverage and
244 observed a genome-wide correlation of 0.89 (Figure 2b).

245

246 We next computed pairwise correlations between the raw coverage for all single cells with each
247 other, with the bulk data, with aggregated published single-cell DamID data (from Kind et al.
248 2015), and with the number of annotated genes in each 250 kb bin genome-wide. We performed
249 unsupervised hierarchical clustering on these datasets and produced a heatmap of their pairwise
250 correlations (Figure 2f). We found that the 3 Dam-only single cells cluster with each other, with
251 the bulk Dam-only data, with the Kind et al. Dam-only data, and with the number of genes, as

252 expected. The 11 Dam-LMNB1 cells cluster separately with each other, with the bulk Dam-
253 LMNB1 data, and with the Kind et al. Dam-LMNB1 data. The anomalous cell #7 shows
254 correlations with both the Dam-only and Dam-LMNB1 clusters, appearing intermediate between
255 them (Figure 2f). This illustrates that our single-cell Dam-LMNB1 and Dam-only cells can be
256 distinguished given their sequencing data alone, and they associate as expected with published
257 data, with our bulk data, and with annotated gene density, further confirming that these sequencing
258 data are measuring meaningful biological patterns in single cells. The anomalous cell #7 can also
259 be distinguished by sequencing data alone, since its data correlate with both the Dam-only and
260 Dam-LMNB1 cell data.

261

262 *μ DamID enables accurate LAD calling within single cells*

263 In order to define LADs across the genome within single cells, we trained a simple classifier on a
264 set of stringent positive and negative controls: regions confidently known to be lamina-associated
265 or not lamina associated based on bulk DamID data from our study and others (Lenain et al. 2017;
266 see Methods). Positive controls consist of 250 kb bins across the genome that were previously
267 annotated in other human cell lines and confirmed with bulk DamID in our own cell line to be
268 consistently associated with the nuclear lamina (referred to as constitutive LADs, or cLADS).
269 Negative controls were similarly determined using prior bulk data to be consistently not associated
270 with the nuclear lamina (referred to as constitutive inter-LADs, or ciLADS). These stringent
271 control sets constitute roughly 10% of the genome each.

272

273 For each single Dam-LMNB1 cell, we computed the distribution of its normalized sequencing
274 coverage in bins from the positive and negative control regions (Figure 2c), with the expectation

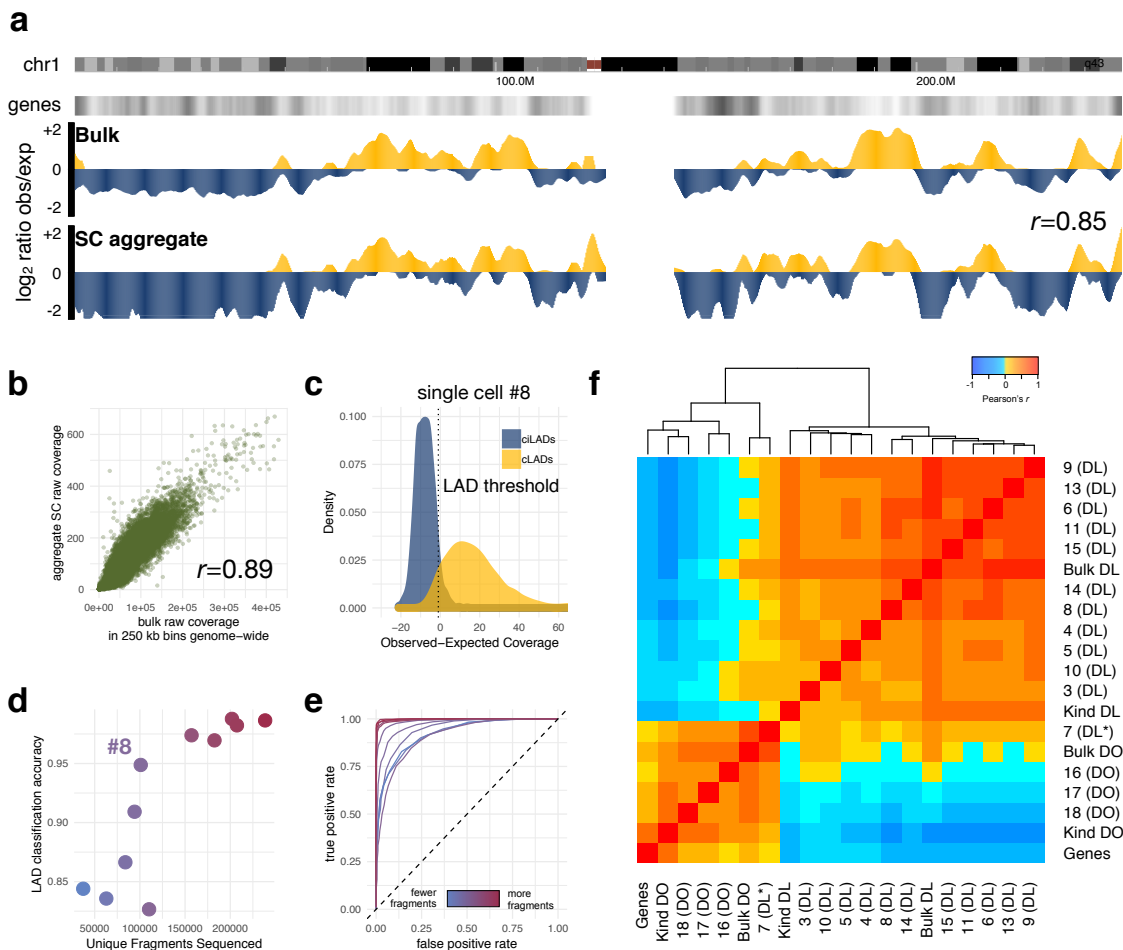


Figure 2. validation of μ DamID sequencing data. (a) comparison of bulk DamID sequencing data and aggregate single-cell sequencing data across all of human chromosome 1. log₂ ratios represent the ratio of Dam-LMN1 sequencing coverage to normalized bulk Dam-only sequencing coverage. Positive values (gold) represent regions associated with the nuclear lamina, which tend to have lower gene density (second track from top). The Pearson correlation between bulk and aggregate single-cell data across all 250-kb bins in the genome is 0.85. (b) scatterplot comparing raw sequencing coverage in bulk and single cell samples (aggregated). (c) normalized coverage distribution in one single cell expressing Dam-LMN1 (cell #8) in positive and negative control sets (cLADs, gold, and ciLADs, blue). The threshold that distinguishes these sets with maximal accuracy is shown as a dotted line. (d) The maximum control set classification accuracy for each of 11 Dam-LMN1 cells versus the number of unique DpnI fragments sequenced for each cell (also indicated by colors). Cell #8, the sample with median accuracy plotted in c, is labeled. (e) Receiver-Operator Characteristic curves for all 11 cells, colored by the number of unique DpnI fragments sequenced. (f) pairwise Pearson correlation heatmap for raw sequencing coverage in 250 kb bins genome-wide, with dendrogram indicating hierarchical clustering results. Numbers indicate cell numbers. DL = Dam-LMN1. DO = Dam-only. Genes = number of Refseq genes in each bin. Kind = aggregated single-cell data from Kind et al. 2015. Bulk = bulk HEK293T DamID data from this study. *anomalous Dam-LMN1 cell (#7) with high m⁶A-tracer signal in the nuclear interior.

297 that ciLADs have little or no coverage and the cLADs have high coverage. Given these control
298 distributions, we chose a coverage threshold to maximally separate the known cLADs and ciLADs.
299 Across the 11 Dam-LMNB1 cells, we determined thresholds that distinguish the known cLADs
300 and ciLADs with a median accuracy of 96% (range 83-99%), which correlates positively with the
301 number of unique DpnI fragments sequenced per cell (Figure 2d). We also plotted receiver
302 operating characteristic (ROC) curves for each cell, showing the empirical tradeoff between false
303 positive and false negative LAD calls at varying thresholds (Figure 2e).

304
305 After choosing a threshold for each cell to maximize classification accuracy between the control
306 sets, we applied these thresholds to make binary LAD classifications across the rest of the genome.
307 At each bin in the genome, we counted the number of Dam-LMNB1 cells in which that bin was
308 classified as an LAD (out of 11 total cells). As expected, bins belonging to the cLAD control sets
309 are classified as LADs in almost all 11 of the cells while bins belonging to the ciLAD control sets
310 are classified as LADs in almost none of the cells (Figure 3a-b). The intermediate bins (called as
311 LADs in 4 to 7 cells), appearing to be lamina associated in only a subset of cells, are likely to
312 contain regions that are variably associated with the lamina, differing from cell to cell, or possibly
313 even dynamically moving between the lamina and the nuclear interior within the same cell over
314 time (Kind et al. 2015). Single-cell data provide a unique opportunity to observe and measure this
315 variability in chromatin organization between cells, enabling the identification of these variable
316 LADs within a population of cells.

317
318 To classify bins confidently as variable LADs, we aimed to rule out the possibility that sampling
319 error could explain the observed intermediate number of LAD-classified cells in these regions,

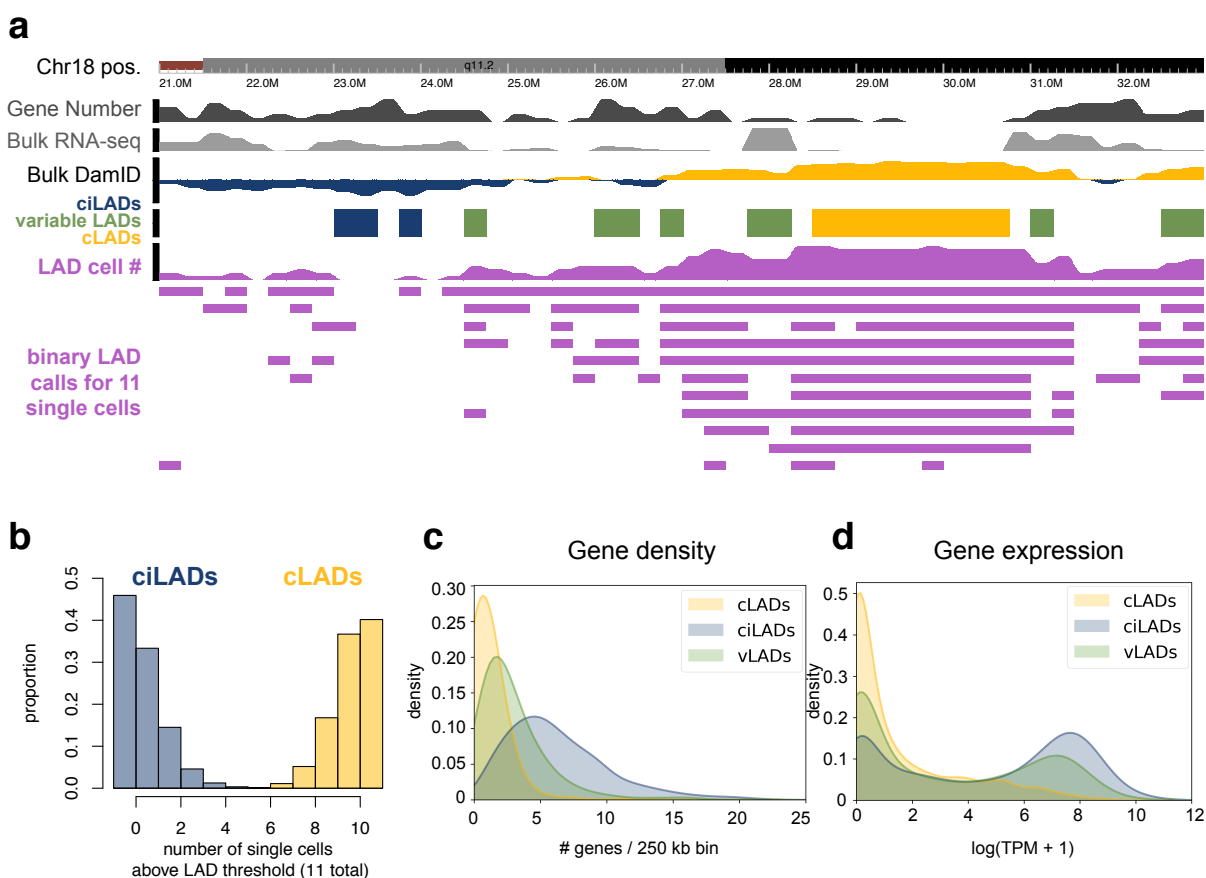


Figure 3. Defining variable LADs in HEK293T cells. (a) A browser screenshot from Chr18:21-33 Mb. The first track shows the chromosome ideogram and coordinates. The second track reports the number of Refseq genes falling in each bin. The third track reports the mean Transcripts Per Million (TPM) value for each gene within each bin from bulk RNA-seq data from untreated HEK293T cells. The fourth track reports the \log_2 FoldChange values from bulk Dam-LMN1:Dam-only sequencing data. The fifth track indicates the positions of the control cLAD (gold) and ciLAD (blue) sets as well as the positions of regions called as variable LADs using the single-cell sequencing data generated here (green). The sixth track shows the number of single cells (out of 11) in which each bin is called as an LAD. Below that, the positions of all bins called as LADs are indicated, with one row per cell. (b) Distribution of the number of single cells (out of 11) in which each bin is called as an LAD for all 250 kb bins genome-wide, separately for each of the control sets of cLADs or ciLADs. (c-d) Distributions of the number of genes (c) or mean TPM per gene (d) per 250 kb bin for each of the sets of cLADs, ciLADs, or variable LADs.

342 given the range of error rates within individual cells. Among bins called as LADs in 4-7 cells, we
343 computed the joint probability of observing that number of cells under two null models: one
344 consisting of true positives and false negatives, and one consisting of true negatives and false
345 positives (see Methods). We selected only the subset of bins with low p-values ($p < 10^{-8}$) under both
346 null models, providing high confidence that these variable LAD regions are truly variable between
347 cells (Figure 3a). We hypothesized that these stringently defined regions, which comprise 13% of
348 the genome, would be more gene rich and have higher gene expression than cLADs, given their
349 dynamic positioning in cells. Indeed, these variable LADs show intermediate gene density and
350 bulk gene expression levels compared to the control sets of cLADs and ciLADs (Figure 3c-d),
351 consistent with these regions being variably active within different cells.

352

353 *μ DamID enables cell-cell comparisons based on imaging and sequencing data*

354 μ DamID enables the joint analysis of the nuclear localization and sequence identity of protein-
355 DNA interactions within each cell and between cells. Because the nuclear localization of LADs is
356 well characterized, one could generate and test hypotheses about the sequencing data given the
357 imaging data for each cell in this study. For example, cells expressing Dam-only show
358 fluorescence throughout the center of the nucleus, and indeed their coverage profiles show little
359 difference in coverage between known cLADs and ciLADs (Figure 4). Moreover, Dam-LMNB1
360 cells with visible rings and low fluorescence in the nuclear interior tend to show well-separated
361 cLAD and ciLAD coverage distributions (Figure 4). One anomalous Dam-LMNB1 cell (cell #7)
362 was selected for having bright fluorescence throughout the nucleus, and its sequencing data
363 confirm that it appears to have increased coverage in ciLADs, appearing like an intermediate
364 between the Dam-only and Dam-LMNB1 coverage signatures (Figure 4). Dam-LMNB1 is likely

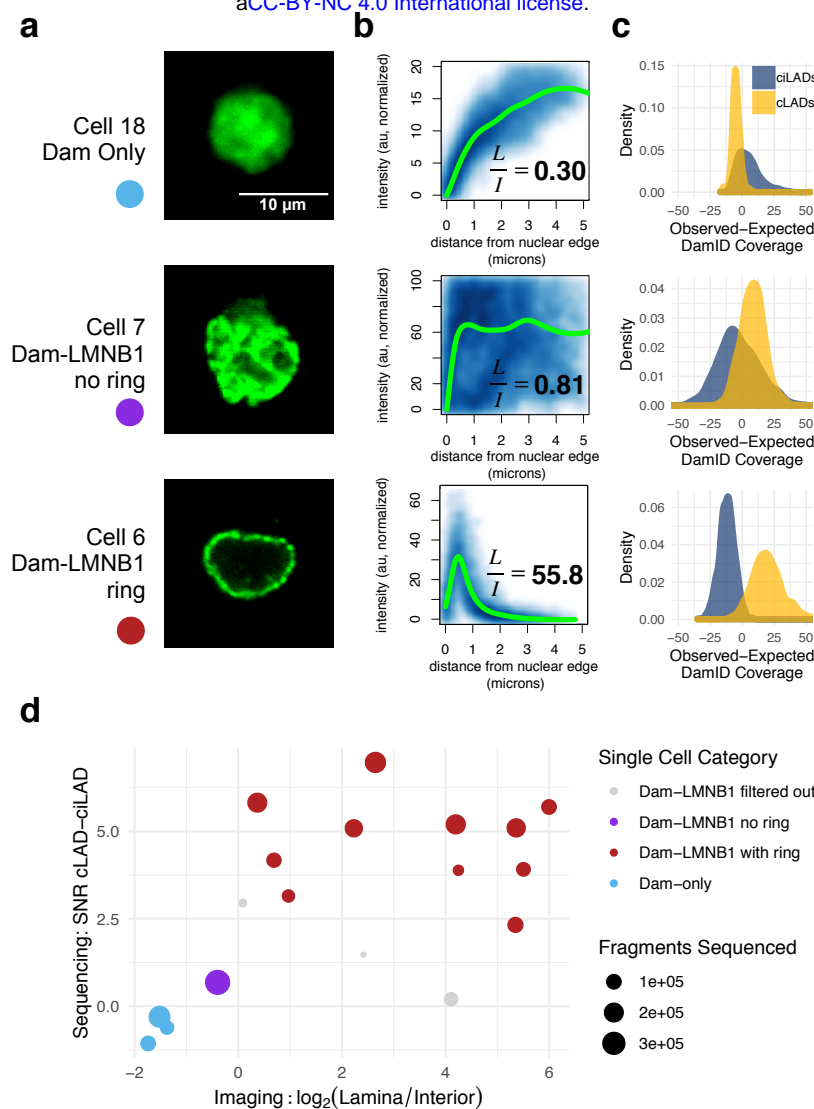


Figure 4. Joint imaging and sequencing analysis with μ DamID. (a) Confocal fluorescence microscopy images of m^6A -Tracer GFP signal from 3 cells: one expressing Dam-only, one expressing Dam-LMNB1 but showing high interior fluorescence, and one expressing Dam-LMNB1 and showing the expected ring-like fluorescence at the nuclear lamina. (b) Normalized pixel intensity values plotted as a function of their distance from the nuclear edge (blue), with a fitted loess curve overlaid (green). Ratios of the mean normalized pixel intensities in the Lamina (<1 micron from the edge) versus the Interior (>3.5 microns from the edge) are printed on each plot. (c) DamID sequencing coverage distributions for each of the cLAD or ciLAD control sets (as in Figure 2c). (d) scatterplot showing sequencing versus imaging metrics for each cell, with point size indicating the number of unique DpnI fragments sequenced for that cell. The x axis reports the \log_2 ratio of the Lamina:Interior mean intensity ratio for each cell. The y axis reports the \log_2 of the Signal-to-Noise Ratio (SNR) computed from the sequencing data for each cell (effectively the difference in means between cLADs and ciLADs divided by the standard deviation of ciLAD coverage).

388 overexpressed in that cell, causing it to accumulate high background levels of methylation
389 throughout the nucleus.

390

391 To quantify these observations across all cells, for each image we generated an averaged GFP
392 intensity profile plot as a function of the distance from the edge of the nuclear lamina (Figure 4b).

393 Using these profiles, we computed the ratio of mean GFP intensity at the nuclear lamina compared
394 to the nuclear interior, which is small for the Dam-only cells and cell #7, and large for the Dam-

395 LMNB1 cells. Then, we compared these imaging ratios to a computed sequencing signal-to-noise
396 ratio (SNR) for each cell, a measure of how well separated the cLAD and ciLAD coverage

397 distributions are (see Methods and Figure 4d). The Dam-only and Dam-LMNB1 cells can be
398 readily separated on either axis, with cell #7 appearing intermediate on both axes. Overall, these

399 data add additional confidence that the sequenced areas correspond to the fluorescing areas of the
400 nucleus, providing two useful measures of chromatin organization within single cells.

401

402

403

404

405

406

407

408

409

410

411 **Conclusions**

412 We have demonstrated the use of an integrated microfluidic device for single-cell isolation,
413 imaging, and sorting, followed by DamID. This system enables the acquisition of paired imaging
414 and sequencing measurements of protein-DNA interactions within single cells, giving a readout of
415 both the ‘geography’ and identity of these interactions in the nucleus. Specifically, we tested the
416 device by mapping well-characterized interactions between DNA and proteins found at the nuclear
417 lamina, providing a measure of genome regulation and 3D chromatin organization within the cell,
418 and recapitulating similar maps in other cell types. This technology could be applied to study many
419 other types of protein-DNA interactions in single cells, and it could be combined with other
420 sequencing and/or imaging modalities to gather even richer information from each cell. For
421 example, the nuclear localization of specific proteins such as heterochromatin-associated proteins
422 or nucleolus-associated proteins can be visualized by fluorescent tagging, then DamID can be used
423 to sequence and identify nearby genomic regions. Recent advances allow for simultaneous DamID
424 and transcriptome sequencing in single cells (Rooijers et al. 2019), and this device could be
425 adapted for similar multi-omic protocols as well. Further improvements to the DamID protocol
426 may also improve its sensitivity and specificity. Finally, one can increase the number of cells
427 processed per batch by scaling up the design and incorporating features like multiplexed valve
428 control and automated image processing and sorting.

429

430

431

432

433

434 **Materials and Methods**

435 *Cell transfection and harvesting*

436 HEK293T cells (CRL-3216, ATCC, Manassas, VA; validated by microsatellite typing, at passage
437 number <10) were seeded in 24-well plates at 50000 cells per well in 0.5 ml media (DMEM plus
438 10% FBS). The next day, cells were transfected using FuGene HD transfection reagent according
439 to their standard protocol for HEK293 cells (Promega, Madison, WI). DNA plasmids were cloned
440 in Dam-negative *E. coli* to reduce sequencing reads originating from plasmid. Dam-LMNB1 and
441 ^{m6}A-Tracer plasmids were obtained from Bas van Steensel (from Kind et al. 2013); Dam-LMNB1
442 was modified to replace GFP with mCherry and to produce a Dam-only version; their sequences
443 are available as supplementary information (see link to GitHub below in Data Availability section).
444 250 ng Dam construct DNA plus 250 ng ^{m6}A-Tracer DNA were used per well. As controls to
445 validate transfection, additional wells were left untransfected, transfected with ^{m6}A-Tracer only,
446 or transfected with Dam construct only. The following day, successful transfection was validated
447 by widefield fluorescence microscopy, seeing GFP signal in wells containing ^{m6}A-Tracer, and
448 mCherry signal in all wells containing Dam construct only. Cells were harvested 72 hours after
449 transfection. 20 hours before harvesting, the media was replaced and 0.5 µl Shield-1 ligand (0.5
450 mM stock, Takara Bio USA, Inc., Mountain View, CA) was added to each well to stabilize protein
451 expression. Cells transfected with Dam-LMNB1 were inspected by fluorescence microscopy to
452 look for the characteristic signal at the nuclear lamina, indicating proper expression and protein
453 activity. To harvest the cells and prepare them for loading on the device, the cells were washed
454 with PBS, then incubated at room temperature with 1X TrypLE Select (ThermoFisher Scientific,
455 Waltham, MA) for 5 minutes to dissociate them from the plate. Cells were pipetted up and down
456 to break up clumps, then centrifuged at 300xg for 5 minutes, resuspended in PBS, centrifuged

457 again, and resuspended in 500 μ l Pick Buffer (50mM Tris-HCl pH 8.3, 75mM KCl, 3mM MgCl₂,
458 137mM NaCl), achieving a final cell concentration of roughly 500,000 cells per ml. Cells were
459 passed through a 40 μ m cell strainer before loading onto the device.

460

461 *Confocal imaging*

462 Fluorescence confocal imaging of cells was performed in the trapping region using an inverted
463 scanning confocal microscope with a 488 nm Ar/Kr laser (Leica, Germany) for excitation, with a
464 bandpass filter capturing backscattered light from 500-540 nm at the primary photomultiplier tube
465 (PMT), with the pinhole set to 1 Airy unit, with a transmission PMT capturing widefield unfiltered
466 forward-scattered light, and with a 63X 0.7 NA long-working-distance air objective with a
467 correction collar, zoomed by scanning 4X. Gain and offset values were set automatically for one
468 cell and identical microscope settings were used to image all cells. The focal plane was positioned
469 in the middle of each nucleus, capturing the largest-circumference cross-section, and final images
470 were averaged over 10 frames to remove noise. The 3 cells expressing Dam-only that were
471 sequenced in this study were imaged with a widefield CCD camera. Other Dam-only cells were
472 imaged with confocal microscopy and showed similar relatively homogenous fluorescence
473 throughout the nucleus, and never the distinct ‘ring’ shape found in Dam-LMNB1 expressing cells
474 (Kind et al. 2013; Supplementary Figure 5). No image enhancement methods were used prior to
475 quantitative image processing. Images in Figures 1 and 4 have been linearly thresholded to
476 diminish background signal.

477

478

479

480 *Mold fabrication*

481 Molds for casting each layer were fabricated on silicon wafers by standard photolithography.
482 Photomasks for each layer were designed in AutoCAD and printed at 25400 DPI (CAD/Art
483 Services, Inc., Bandon, Oregon). The mask for the thick layer, in this case the flow layer to make
484 push-up valves, was scaled up in size uniformly by 1.5% to account for thick layer shrinkage. A
485 darkfield mask was used for features made out of negative photoresist: the filters on the flow layer
486 and the entire control layer; a brightfield mask was used for all flow layer channels, which were
487 made out of positive photoresist (mask designs available on GitHub; see Data Availability section
488 below). 10 cm diameter, 500 μm thick test-grade silicon wafers (item #452, University Wafer,
489 Boston, MA) were cleaned by washing with 100% acetone, then 100% isopropanol, then DI water,
490 followed by drying with an air gun, and heating at 200°C for 5 minutes.

491
492 To make the control layer mold, SU-8 2025 negative photoresist (MicroChem Corp.,
493 Westborough, MA) was spin-coated to achieve 25 μm thickness (7 s at 500 rpm with 100 rpm/s
494 ramp, then 30 s at 3500 rpm with 300 rpm/s ramp). All baking temperatures, baking times,
495 exposure dosages, and development times followed the MicroChem data sheet. All baking steps
496 were performed on pre-heated ceramic hotplates. After soft-baking, the wafer was exposed beneath
497 the darkfield control layer mask using a UV aligner (OAI, San Jose, CA). After post-exposure
498 baking and development, the mold was hard-baked at 150°C for 5 minutes.

499
500 To make the flow layer mold, first the filters were patterned with SU-8 2025, which was required
501 to make fine, high-aspect-ratio filter features that would not re-flow at high temperatures. SU-8
502 2025 was spin-coated to achieve 40 μm thickness (as above but with 2000 rpm final speed) and

503 processed according to the MicroChem datasheet as above, followed by an identical hard-bake
504 step. Next, AZ 40XT-11D positive photoresist (Integrated Micro Materials, Argyle, TX) was spin-
505 coated on top of the SU-8 features to achieve 20 μm thickness across the wafer (as above but with
506 3000 rpm final speed). All baking temperatures, baking times, exposure dosages, and development
507 times followed the AZ 40XT-11D data sheet. After development, the channels were rounded by
508 reflowing the photoresist, achieved by placing the wafer at 65°C for 1 min, then 95°C for 1 min,
509 then 140°C for 1 min followed by cooling at room temperature. In our experience, reflowing for
510 too long, or attempting to hard-bake the AZ 40XT-11D resulted in undesirable ‘beading’ of the
511 resist, especially at channel junctions. Because it was not hard-baked, no organic solvents were
512 used to clean the resulting mold. Any undeveloped AZ 40XT-11D trapped in the filter regions was
513 carefully removed using 100% acetone applied locally with a cotton swab.

514

515 *Soft lithography*

516 Devices were fabricated by multilayer soft lithography (Unger et al. 2000). On-ratio 10:1
517 base:crosslinker RTV615A PDMS (Momentive Performance Materials, Inc., Waterford, NY) was
518 used for both layers, and layer bonding was performed by partial curing, followed by alignment,
519 then full curing (Lai et al. 2019). To prevent PDMS adhesion to the molds, the molds were
520 silanized by exposure to trichloromethylsilane (Sigma-Aldrich, St. Louis, MO) vapor under
521 vacuum for 20 min. PDMS base and crosslinker were thoroughly mixed by an overhead mixer for
522 2 minutes, then degassed under vacuum for 90 minutes. Degassed PDMS was spin-coated on the
523 control layer mold (for the ‘thin layer’) to achieve a thickness of 55 μm (7 s at 500 rpm with 100
524 rpm/s ramp, then 60 s at 2000 rpm with 500 rpm/s ramp), then placed in a covered glass petri dish
525 and baked for 10 minutes at 70°C in a forced-air convection oven (Heratherm OMH60, Thermo

526 Fisher Scientific, Waltham, MA) to achieve partial curing. The flow layer mold (for the ‘thick
527 layer’) was placed in a covered glass petri dish lined with foil, and degassed PDMS was poured
528 onto it to a depth of 5 mm. Any bubbles were removed by air gun or additional degassing under
529 vacuum for 5 minutes, then the thick layer was baked for 19 minutes at 70°C. Holes were punched
530 using a precision punch with a 0.69 mm punch tip (Accu-Punch MP10 with CR0420275N19R1
531 punch, Syneo, Angleton, TX). The thick layer was peeled off the mold, cut to the edges of the
532 device, and aligned manually under a stereoscope on top of the thin layer, which was still on its
533 mold. The layers were then fully cured and bonded together by baking at 70°C for 120 min. After
534 cooling, the devices were peeled off the mold, and the inlets on the thin layer were punched. The
535 final devices were bonded to 1 mm thick glass slides, which were first cleaned by the same method
536 as used for silicon wafers above, using oxygen plasma reactive ion etching (20 W for 23 s at 285
537 Pa pressure; Plasma Equipment Technical Services, Brentwood, CA), followed by heating at
538 100°C on a ceramic hot plate for 5 minutes.

539

540 *Device and control hardware setup*

541 Devices were pneumatically controlled by a solenoid valve manifold (Pneumadyne, Plymouth,
542 MN). Each three-way, normally open solenoid valve switched between a regulated and filtered
543 pressure source inlet at 25 psi (172 kPa) or ambient pressure to close or open microfluidic valves,
544 respectively. Solenoid valves were controlled by the KATARA control board and software (White
545 and Streets 2018). Most operational steps were carried out on inverted microscopes using 4-10X
546 objectives. For incubation steps, the device was placed on a custom-built liquid-cooled
547 thermoelectric temperature control module (TC-36-25-RS232 PID controller with a 36 V 16 A
548 power source and two serially connected VT-199-1.4-0.8P TE modules and an MP-3022

549 thermistor; TE technologies, Traverse City, MI) controlled by a new KATARA software module
550 (to be made available on github). A layer of mineral oil was applied between the chip and the
551 temperature controller to improve thermal conductivity and uniformity. A stereoscope was used to
552 monitor the chip while on the temperature controller.

553

554 To set up each new device, each pneumatic valve was connected to one control inlet on the
555 microfluidic device by serially connecting polyurethane tubing (3/32" ID, 5/32" OD;
556 Pneumadyne) to Tygon tubing (0.5 mm ID, 1.5 mm OD) to >4 cm PEEK tubing (0.25 mm ID, 0.8
557 mm OD; IDEX Corporation, Lake Forest, IL). Solenoid valves were energized to de-pressurize
558 the tubing and the tubing was primed by injecting water using a syringe connected to the end of
559 the PEEK tubing, then the primed PEEK tubing was inserted directly into each punched inlet hole
560 on the device. Solenoid valves were de-energized to pressurize the tubing until all control channels
561 on the device were fully dead-end filled, then each microfluidic valve was tested and inspected by
562 switching on and off its corresponding solenoid valve. All valves were opened and the device was
563 passivated by filling all flow-layer channels with syringe-filtered 0.2% (w/w) Pluronic F-127
564 solution (P2443; MilliporeSigma, St. Louis, MO) from the reagent inlet and incubating at room
565 temperature for 1 hour. The device was then washed by flowing through 0.5 ml of ultra-filtered
566 water, followed by air to dry it.

567

568 *Device operation*

569 Initially, all chamber valves and reagent inlet valves were closed. Gel-loading pipette tips were
570 used to inject reagents and cells into the flow channels. To prepare the device for operation, pick
571 buffer was injected into the reagent inlet and pressurized at 5-10 psi to dead-end fill the reagent

572 inlet channels. Negative controls were generated by injecting pure pick buffer into one of the
573 holding chambers before trapping and sorting cells into the other lanes. 50 μ l of cell suspension
574 was then loaded into a gel-loading pipette tip, and injected directly into the cell inlet. A high-
575 precision pressure regulator was used to load the single-cell suspension at 1 psi (7 kPa). Cells were
576 observed in the filter region with brightfield and epifluorescence using a 10X objective to identify
577 candidate cells. These were then tracked through the device until they approached the trapping
578 chamber for an empty lane. To trap a candidate cell, the device's peristaltic pump was operated at
579 1 Hz to deliver that cell to the trap region. The trap valves (above and below the trap region; see
580 Figure S1) were closed and the cell was imaged with scanning confocal microscopy as described
581 above. If the cell was rejected after imaging, the trap valves were opened and it was flushed to the
582 waste outlet. Otherwise, the cell was injected into the holding chamber by dead-end filling. This
583 process was repeated to fill each lane with single cells for DamID. To test background DNA levels,
584 we filled the final lane with only cell suspension buffer. Nearly undetectable levels of amplified
585 DNA were recovered from these lanes.

586

587 After filling all 10 lanes, the reagent inlet and cell trapping channels were flushed with 0.5 ml of
588 water, which exited through the waste outlet and the cell inlet, to remove any remaining Pick buffer
589 or cell debris, then air dried. The same washing and drying was repeated between each reaction
590 step. To inject reagents for each reaction of the DamID protocol, the trap valves were closed, the
591 reagent channels were dead-end filled with freshly prepared and syringe-filtered reagent, then the
592 reagent inlet valves and the valves for the necessary reaction chambers were opened, and each lane
593 was dead-end filled individually to prevent any possible cross-contamination. Reaction contents
594 are described in Table 1.

595 After filling all lanes, reagents were mixed by actuating the chamber valves at 5 Hz for 5 minutes.
 596 At the PCR step, rotary mixing was achieved by using the chamber valves to make a peristaltic
 597 pump driving fluid around the full reaction ring. For each reaction step, the device was placed on
 598 the thermal controller and reactions were with times and temperatures described in Table 1. PCR
 599 thermocycling conditions are described in Table 2. To ensure adequate hydration during PCR, all
 600 valves were pressurized. Amplified DNA was flushed out of each lane individually using purified
 601 water from the reagent inlet, collected into a gel loading tip placed in the lane outlet to a final
 602 volume of 5 μ l then transferred to a 0.2 ml PCR strip tube.

603

604 **Table 1. Reaction buffers and conditions**

Reaction Stage	Buffer	Incubation
Trapping & Holding	<u>Pick Buffer:</u> 50mM Tris-HCl pH 8.3 75mM KCl, 3mM MgCl ₂ 137mM NaCl	RT
Lysis	10mM TRIS acetate pH 7.5 10mM magnesium acetate 50mM potassium acetate 0.67% Tween-20 0.67% Igepal 0.67 mg/ml proteinase K	42 °C for 4 hours then 80 °C for 10 min
Digestion	mix 7 μ l 10X Cutsmart buffer 1 μ l DpnI (New England Biolabs, Ipswich, MA) 62 μ l H ₂ O	37 °C for 4 hours then 80 °C for 20 min
Ligation	mix 6 μ l 10X NEB T4 ligase buffer 1 μ l DamID adapter stock at 25 μ M 0.2 μ l NEB T4 ligase at 400 U/ μ l 21.8 μ l H ₂ O 1 μ l 2% w/v Tween-20	16 °C overnight then 65 °C for 10 min
PCR	from Takara Clontech Advantage 2 kit: mix 5 μ l 10X PCR buffer 1 μ l dNTPs at 10 mM each 1 μ l polymerase mix 0.63 μ l DamID primer 21.37 μ l H ₂ O 1 μ l 2% Tween-20	See Table 2

605

606

607 **Table 2. PCR thermocycling conditions**

PCR Step	Incubation
1	68 °C for 10 min
2	94 °C for 1 min
3	65 °C for 5 min
4	68 °C for 15 min
5	94 °C for 1 min
6	65 °C for 1 min
7	68 °C for 10 min
8	Go to step 5 (x 3)
9	94 °C for 1 min
10	65 °C for 1 min
11	68 °C for 2 min
12	Go to step 9 (x 22)
13	Hold 10 °C

608

609 *Oligonucleotides*

610 >AdRt
611 CTAATACGACTCACTATAGGGCAGCGTGGTCGCGGCCGAGGA
612 >AdRb
613 TCCTCGGCCG
614 >AdR_PCR
615 NNNNGTGGTCGCGGCCGAGGATC
616

617 To anneal DamID adapter (from Vogel et al. 2007): mix equal volumes of 50 µM AdRt and 50
618 µM AdRb in a microcentrifuge tube, then fully submerge it in a beaker of boiling water, and allow
619 the water to equilibrate to room temperature slowly.

620

621

622 *Quality control, library preparation, and sequencing*

623 Samples were diluted to 10 μ l total volume and two replicates of qPCR were performed using the
624 DamID PCR primer to estimate DNA quantities relative to the pick-buffer-only negative control
625 (1 μ l DNA per replicate in 10 μ l reaction volume). We also used 1 μ l of sample to measure DNA
626 concentration using a Qubit fluorometer with a High-Sensitivity DNA reagent kit (quantitative
627 range 0.2 ng – 100 ng; ThermoFisher Scientific). Samples with the lowest Ct values and highest
628 Qubit DNA measurements were selected for library preparation and sequencing. Library
629 preparation was carried out using an NEBNext Ultra II DNA Library Prep Kit for Illumina (NEB
630 E7645) with dual-indexed multiplex i5/i7 oligo adapters. Size selection was not performed; PCR
631 was carried out for 9 cycles. Libraries were quantified again by Qubit and size profiled on a
632 TapeStation 4200 with a D5000 HS kit (Agilent, Santa Clara, CA), then mixed to achieve
633 equimolar amounts of each library. DNA was sequenced on an Illumina MiniSeq with a 150-cycle
634 high output kit, to produce paired 75 bp reads, according to manufacturer instructions (Illumina,
635 San Diego, CA). Roughly 13 million read pairs were obtained.

636

637 *Bulk DamID*

638 Genomic DNA was isolated from $\sim 3.7 \times 10^6$ transfected HEK293T cells using the DNeasy Blood
639 & Tissue kit (Qiagen) following the protocol for cultured animal cells with the addition of RNase
640 A. The extracted gDNA was then precipitated by adding 2 volumes of 100% ethanol and 0.1
641 volume of 3 M sodium acetate (pH 5.5) and storing at -20 $^{\circ}$ C for 30 minutes. Next, centrifugation
642 for 30 minutes at 4 $^{\circ}$ C, $>16,000 \times g$ was performed to spin down the gDNA. The supernatant was
643 removed, and the pellet was washed by adding 1 volume of 70% ethanol. Centrifugation for 5
644 minutes at 4 $^{\circ}$ C, $>16,000 \times g$ was performed, the supernatant was removed, and the gDNA pellets

645 were air-dried. The gDNA was dissolved in 10 mM Tris-HCl pH 7.5, 0.1 mM EDTA to 1 µg/µl,
646 incubating at 55 °C for 30 minutes to facilitate dissolving. The concentration was measured using
647 Nanodrop.

648

649 The following DpnI digestion, adaptor ligation, and DpnII digestion steps were all performed in
650 the same tube. Overnight DpnI digestion at 37 °C was performed with 2.5 µg gDNA, 10 U DpnI
651 (NEB), 1X CutSmart (NEB), and water to 10 µl total reaction volume. DpnI was then inactivated
652 at 80 °C for 20 minutes. Adaptors were ligated by combining the 10 µl of DpnI-digested gDNA,
653 1X ligation buffer (NEB), 2 µM adaptor dsAdR, 5 U T4 ligase (NEB), and water for a total reaction
654 volume of 20 µl. Ligation was performed for 2 hours at 16 °C and then T4 ligase was inactivated
655 for 10 minutes at 65 °C. DpnII digestion was performed by combining the 20 µl of ligated DNA,
656 10 U DpnII (NEB), 1X DpnII buffer (NEB), and water for a total reaction volume of 50 µl. The
657 DpnII digestion was 1 hour at 37 °C followed by 20 minutes at 65 °C to inactivate DpnII.

658

659 Next, 10 µl of the DpnII-digested gDNA was amplified using the Clontech Advantage 2 PCR Kit
660 with 1X SA PCR buffer, 1.25 µM Primer Adr-PCR, dNTP mix (0.2 mM each), 1X PCR advantage
661 enzyme mix, and water for a total reaction volume of 50 µl. PCR was performed with an initial
662 extension at 68 °C for 10 minutes; one cycle of 94 °C for 1 minute, 65 °C for 5 minutes, 68 °C for
663 15 minutes; 4 cycles of 94 °C for 1 minute, 65 °C for 1 minute, 68 °C for 10 minutes; 21 cycles of
664 94 °C for 1 minute, 65 °C for 1 minute, 68 °C for 2 minutes. Post-amplification DpnII digestion
665 was performed by combining 40 µl of the PCR product with 20 U DpnII, 1X DpnII buffer, and
666 water to a total volume of 100 µl. The DpnII digestion was performed for 2 hours at 37 °C followed

667 by inactivation at 65 °C for 20 minutes. The digested product was purified using QIAquick PCR
668 purification kit.

669

670 The purified PCR product (1 µg brought up to 50 µl in TE) was sheared to a target size of 200 bp
671 using the Bioruptor Pico with 13 cycles with 30"/30" on/off cycle time. DNA library preparation
672 of the sheared DNA was performed using NEBNext Ultra II DNA Library Prep Kit for Illumina.

673

674 *Bulk DamID, comparing Dam mutants*

675 Bulk DamID for comparing the wild-type allele and V133A mutant allele was performed as
676 outlined in the Bulk DamID methods section with the following modifications. Genomic DNA
677 was extracted from ~ 2.4 x 10⁵ transfected HEK293T cells. A cleanup before methylation-specific
678 amplification was included to remove unligated Dam adapter before PCR. The Monarch PCR &
679 DNA Cleanup Kit with 20 µl DpnII-digested gDNA input and an elution volume of 10 µl was
680 used. Shearing with the Bioruptor Pico was performed for 20 total cycles with 30"/30" on/off cycle
681 time. Paired-end 2 x 75 bp sequencing was performed on an Illumina NextSeq with a mid output
682 kit. Approximately 3.8 million read pairs per sample were obtained.

683

684 *Bulk RNA-seq*

685 RNA was extracted from ~1.9 x 10⁶ transfected HEK293T cells using the RNeasy Mini Kit from
686 Qiagen with the QIAshredder for homogenization. RNA library preparation was performed using
687 the NEBNext Ultra II RNA Library Prep Kit for Illumina with the NEBNext Poly(A) mRNA
688 Magnetic Isolation Module. Paired-end 2 x 150 bp sequencing for both DamID-seq and RNA-seq
689 libraries was performed on 1 lane of a NovaSeq S4 run. Approximately 252 million read pairs

690 were obtained for each DamID-seq sample, and roughly 64 million read pairs for each RNA
691 sample. Adapters were trimmed using trimmomatic (v0.39; Bolger et al. 2014;
692 ILLUMINACLIP:adapters-PE.fa:2:30:10 LEADING:3 TRAILING:3 SLIDINGWINDOW:4:15
693 MINLEN:36, where adapters-PE.fa is:

```
694     >PrefixPE/1  
695     TACTCTTTCCCTACACGACGCTCTTCCGATCT  
696     >PrefixPE/2  
697     GTGACTGGAGTTCAGACGTGTGCTCTTCCGATCT).
```

699 Transcript quantification was performed using Salmon (Patro et al. 2017) with the GRCh38
700 transcript reference. Differential expression analysis was performed using the voom function in
701 limma (Ritchie et al. 2015). Differential expression was called based on logFC significantly greater
702 than 1 and adjusted p-value < 0.01.

703

704 *DamID sequence processing and analysis*

705 Bulk and single-cell DamID reads were demultiplexed using Illumina's BaseSpace platform to
706 obtain fastq files for each sample. DamID and Illumina adapter sequences were trimmed off using
707 trimmomatic (v0.39; Bolger et al. 2014; ILLUMINACLIP:adapters-PE.fa:2:30:10 LEADING:3
708 TRAILING:3 SLIDINGWINDOW:4:15 MINLEN:20, where adapters-PE.fa is:

```
709     >PrefixPE/1  
710     TACTCTTTCCCTACACGACGCTCTTCCGATCT  
711     >PrefixPE/2  
712     GTGACTGGAGTTCAGACGTGTGCTCTTCCGATCT).  
713     >Dam  
714     GGTCGCGGCCGAGGA  
715     >Dam_rc  
716     TCCTCGGCCGCGACC
```

717). Trimmed reads were aligned to a custom reference (hg38 reference sequence plus the Dam-
718 LMNB1 and ^{m6}A-Tracer plasmid sequences) using BWA-MEM (v0.7.15-r1140, Li 2013).

719 Alignments with mapping quality 0 were discarded using samtools (v1.9, Li et al. 2009). The hg38
720 reference sequence was split into simulated DpnI digestion fragments by reporting all intervals
721 between GATC sites (excluding the GATC sites themselves), yielding 7180359 possible DpnI
722 fragments across the 24 chromosome assemblies. The number of reads overlapping each fragment
723 was counted using bedtools (v2.28; Quinlan et al. 2010). For single-cell data, the number of DpnI
724 fragments with non-zero coverage was reported within each non-overlapping bin in the genome
725 (11512 total 250 kb bins). For bulk data, the number of read pairs overlapping each 250 kb bin
726 was reported. The same exact pipeline was applied to the raw reads from Kind et al. 2015 in
727 aggregate. RefSeq gene positions were downloaded from the UCSC Genome Browser and counted
728 in each bin. For bulk data, Dam-LMNB1 vs DamOnly enrichment was computed using DEseq2 in
729 each 250 kb bin (Love et al. 2014). For single-cell data, the expected background coverage in each
730 bin was computed as $n(m/t)$, where n is the number of unique fragments sequenced from that cell,
731 m is the number of bulk Dam-only read pairs mapping to that bin, and t is the total number of
732 mapped bulk Dam-only read pairs. Single-cell normalization was computed either as a ratio of
733 observed to expected coverage (for browser visualization and comparison to bulk data), or as their
734 difference (for classification and coverage distribution plotting). Positive and negative control sets
735 of cLAD and ciLAD bins were defined as those with a bulk Dam-LMNB1:Dam-only DEseq2 p-
736 value smaller than 0.01/11512, that intersected published cLADs and ciLADs in other cell lines
737 (Lenain et al. 2017), and that were among the top 1200 most differentially enriched bins in either
738 direction (positive or negative log fold change for cLADs and ciLADs, respectively). Integer
739 normalized coverage thresholds for LAD/iLAD classification were computed for each cell to
740 maximize accuracy on the cLAD and ciLAD control sets. Signal-to-noise ratios were computed
741 for each cell using the normalized coverage distributions in the cLAD and ciLAD control sets as

742 $(\mu_{\text{cLAD}} - \mu_{\text{ciLAD}})/\sigma_{\text{ciLAD}}$. Statistical analyses and plots were made in R (v3.5.2) using the ggplot2
743 (v3.1.0), gplots (v3.0.1.1), and colorRamps (v2.3) packages. Browser figures were generated using
744 the WashU Epigenome Browser (Li et al. 2019).

745

746 *Image processing*

747 Images were processed in R (v3.5.2) and plots were produced using the reshape2 (v1.4.3),
748 SDMTTools (v1.1-221.1), spatstat (v1.59-0), magick (v2.0), ggplot2 (v3.1.0), and ggbeeswarm
749 (v0.6) packages. Grayscale images were converted to numeric matrices and edge detection was
750 performed using Canny edge detection using the image_canny function in magick, varying the
751 geometry parameters manually for each cell. The center of mass of all edge points was obtained,
752 and all edge points were plotted in Cartesian coordinated with this center of mass as the origin.
753 Noise was removed by removing points with a nearest neighbor more than 2 microns away. Edge
754 point coordinates were converted to polar coordinates, and the farthest points from the origin in
755 each 10 degree arc were reported. Within each 10 degree arc, all pixel intensities from the original
756 image within the edges of the nucleus were reported as a function of their distance from the farthest
757 edge point in that arc to make Figure 4b. For each cell a loess curve (span 0.3) was fitted to the
758 data after subtracting the minimum intensity value within 3.5 microns of the edge. The
759 Lamina:Interior ratio was computed as the ratio of mean intensity of pixels within 1 micron of the
760 edge to the mean intensity of pixels more than 3.5 microns from the edge, after subtracting the
761 minimum value of the loess curve for that cell.

762

763

764

765 **Author contributions**

766 NA and AMS conceived of and designed the study and the microfluidic device. NA and AL
767 fabricated and optimized operation of the device. AM performed bulk cell experiments and data
768 processing, and NA performed all other experiments, analysis, and pneumatic/thermoelectric
769 hardware construction. JAW developed the microfluidic control platform and thermal cycling
770 software, with minor modifications by NA. NA wrote the manuscript with contribution from AM
771 and AMS. AMS supervised the study.

772

773 **Acknowledgements**

774 We would like to thank Anushka Gupta, Gabriel Dorlhiac, Zoë Steier, Adam Gayoso, Tyler Chen,
775 Xinyi Zhang, and Carolina Rioz-Martinez for their helpful feedback on this work. We are grateful
776 to Carolyn de Graaf for providing us with LAD coordinates, to Bo Huang for providing guidance
777 and materials, and to Bas van Steensel for providing us with plasmids. Nicolas Altemose is
778 supported by a Howard Hughes Medical Institute Gilliam Fellowship for Advanced Study. This
779 work was supported by the National Institute of General Medical Sciences of the National
780 Institutes of Health [Grant Number R35GM124916]. Aaron M. Streets is a Chan Zuckerberg
781 Biohub Investigator.

782

783 **Conflicts of interest**

784 The authors declare no competing interests.

785

786

787

788 **Data availability**

789 Sequencing data are available on FigShare: <https://doi.org/10.6084/m9.figshare.8856368>.

790 Imaging data are available on FigShare: <https://doi.org/10.6084/m9.figshare.8940245>.

791 Analysis code, control software, device design files, and plasmid sequences are available on

792 GitHub: <https://github.com/altemose/microDamID>.

793

794

795

796

797

798

799

800

801

802

803

804

805

806

807

808

809

810

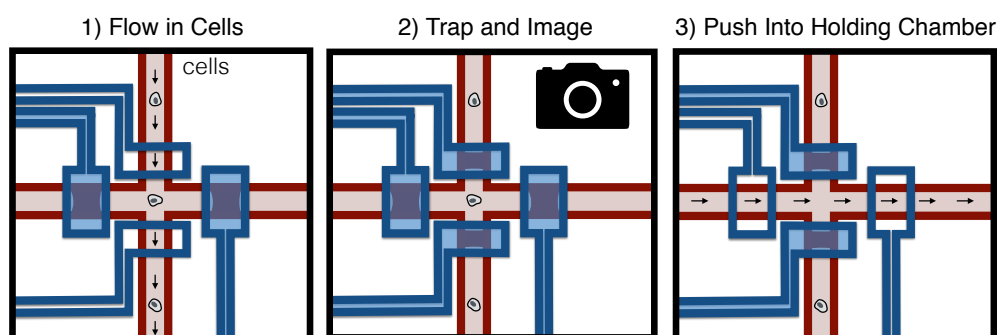
811 References

- 812 Aughey, G. N., & Southall, T. D. (2016). Dam it's good! DamID profiling of protein-DNA
813 interactions. *Wiley Interdisciplinary Reviews: Developmental Biology*, 5(1), 25–37.
814 <http://doi.org/10.1002/wdev.205>
- 815 Aughey, G. N., Gomez, A. E., Thomson, J., Yin, H., & Southall, T. D. (2018). CATaDa reveals
816 global remodelling of chromatin accessibility during stem cell differentiation in vivo. *eLife*, 7.
817 <http://doi.org/10.7554/eLife.32341>
- 818 Bickmore, W. A., & van Steensel, B. (2013). Genome architecture: domain organization of
819 interphase chromosomes. *Cell*, 152(6), 1270–1284. <http://doi.org/10.1016/j.cell.2013.02.001>
- 820 Bolger, A. M., Lohse, M., & Usadel, B. (2014). Trimmomatic: a flexible trimmer for Illumina
821 sequence data. *Bioinformatics (Oxford, England)*, 30(15), 2114–2120.
822 <http://doi.org/10.1093/bioinformatics/btu170>
- 823 Buchwalter, A., Kaneshiro, J. M., & Hetzer, M. W. (2018). Coaching from the sidelines: the
824 nuclear periphery in genome regulation. *Nature Reviews Genetics*, 1–12.
825 <http://doi.org/10.1038/s41576-018-0063-5>
- 826 Carter, B., Ku, W. L., Tang, Q., Kang, J. Y., & Zhao, K. (2019). Mapping Histone Modifications
827 in Low Cell Number and Single Cells Using Antibody-guided Chromatin Tagmentation (ACT-
828 seq). *bioRxiv*, 571208. <http://doi.org/10.1101/571208>
- 829 Elsayy, H., & Chahar, S. (2014). Increasing DNA substrate specificity of the EcoDam DNA-
830 (adenine N(6))-methyltransferase by site-directed mutagenesis. *Biochemistry. Biokhimiia*,
831 79(11), 1262–1266. <http://doi.org/10.1134/S0006297914110145>
- 832 ENCODE Consortium (2012). An integrated encyclopedia of DNA elements in the human
833 genome. *Nature*, 489(7414), 57–74. <http://doi.org/10.1038/nature11247>
- 834 Grosselin, K., Durand, A., Marsolier, J., Poitou, A., Marangoni, E., Nemati, F., et al. (2019). High-
835 throughput single-cell ChIP-seq identifies heterogeneity of chromatin states in breast cancer.
836 *Nature Publishing Group*, 51(6), 1060–1066. <http://doi.org/10.1038/s41588-019-0424-9>
- 837 Guelen, L., Pagie, L., Brasset, E., Meuleman, W., Faza, M. B., Talhout, W., et al. (2008). Domain
838 organization of human chromosomes revealed by mapping of nuclear lamina interactions.
839 *Nature*, 453(7197), 948–951. <http://doi.org/10.1038/nature06947>
- 840 Harada, A., Maehara, K., Handa, T., Arimura, Y., Nogami, J., Hayashi-Takanaka, Y., et al. (2018).
841 A chromatin integration labelling method enables epigenomic profiling with lower input.
842 *Nature Cell Biology*, 1. <http://doi.org/10.1038/s41556-018-0248-3>
- 843 Jakobsen, J. S., Bagger, F. O., Hasemann, M. S., Schuster, M. B., Frank, A.-K., Waage, J., et al.
844 (2015). Amplification of pico-scale DNA mediated by bacterial carrier DNA for small-cell-
845 number transcription factor ChIP-seq. *BMC Genomics*, 16(1), 46.
846 <http://doi.org/10.1186/s12864-014-1195-4>
- 847 Johnson, D. S., Mortazavi, A., Myers, R. M., & Wold, B. (2007). Genome-wide mapping of in
848 vivo protein-DNA interactions. *Science (New York, NY)*, 316(5830), 1497–1502.
849 <http://doi.org/10.1126/science.1141319>
- 850 Kaya-Okur, H. S., Wu, S. J., Codomo, C. A., Pledger, E. S., Bryson, T. D., Henikoff, J. G., et al.
851 (2019). CUT&Tag for efficient epigenomic profiling of small samples and single cells. *Nature*
852 *Communications*, 10(1), 1930. <https://doi.org/10.1038/s41467-019-09982-5>
- 853 Kelsey, G., Stegle, O., & Reik, W. (2017). Single-cell epigenomics: Recording the past and
854 predicting the future. *Science (New York, NY)*, 358(6359), 69–75.
855 <http://doi.org/10.1126/science.aan6826>

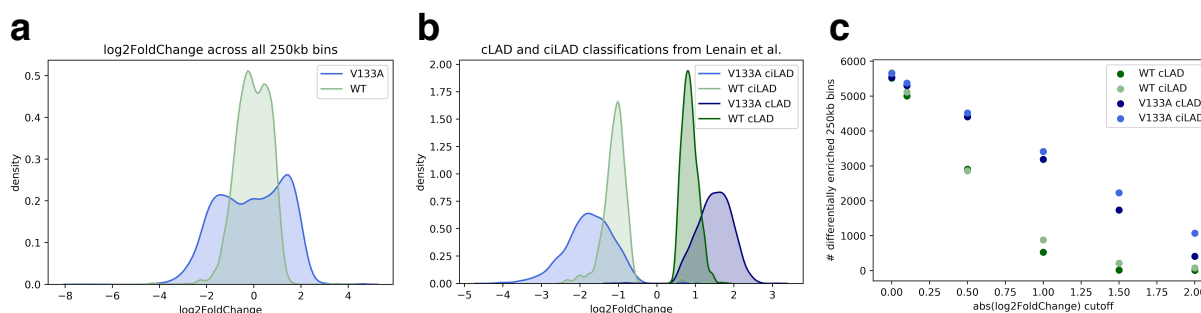
- 856 Kind, J., Pagie, L., Ortabozkoyun, H., Boyle, S., de Vries, S. S., Janssen, H., et al. (2013). Single-
857 cell dynamics of genome-nuclear lamina interactions. *Cell*, 153(1), 178–192.
858 <http://doi.org/10.1016/j.cell.2013.02.028>
- 859 Kind, J., Pagie, L., de Vries, S. S., Nahidiazar, L., Dey, S. S., Bienko, M., et al. (2015). Genome-
860 wide maps of nuclear lamina interactions in single human cells. *Cell*, 163(1), 134–147.
861 <http://doi.org/10.1016/j.cell.2015.08.040>
- 862 Lai, A., Altemose, N., White, J. A., & Streets, A. M. (2018). On-ratio PDMS bonding for
863 multilayer microfluidic device fabrication. *bioRxiv*, 450544. <http://doi.org/10.1101/450544>
- 864 Lenain, C., de Graaf, C. A., Pagie, L., Visser, N. L., de Haas, M., de Vries, S. S., et al. (2017).
865 Massive reshaping of genome–nuclear lamina interactions during oncogene-induced
866 senescence. *Genome Research*. <http://doi.org/10.1101/gr.225763.117>
- 867 Li, D., Hsu, S., Purushotham, D., et al. (2019). WashU Epigenome Browser update 2019. *Nucleic
868 Acids Research*, gkz348, <https://doi.org/10.1093/nar/gkz348>
- 869 Li, H. (2013). Aligning sequence reads, clone sequences and assembly contigs with BWA-MEM.
870 *arXiv*. <https://arxiv.org/abs/1303.3997v2>
- 871 Li, H., Handsaker, B., Wysoker, A., Fennell, T., Ruan, J., Homer, N., et al. (2009). The Sequence
872 Alignment/Map format and SAMtools. *Bioinformatics (Oxford, England)*, 25(16), 2078–2079.
873 <http://doi.org/10.1093/bioinformatics/btp352>
- 874 Love, M. I., Huber, W., & Anders, S. (2014). Moderated estimation of fold change and dispersion
875 for RNA-seq data with DESeq2. *Genome Biology*, 15(12), 550. <http://doi.org/10.1186/s13059-014-0550-8>
- 877 O'Brown, Z. K., Boulias, K., Wang, J., Wang, S. Y., O'Brown, N. M., Hao, Z., et al. (2019).
878 Sources of artifact in measurements of 6mA and 4mC abundance in eukaryotic genomic DNA.
879 *BMC Genomics*, 20(1), 445. <http://doi.org/10.1186/s12864-019-5754-6>
- 880 Orian, A., van Steensel, B., Delrow, J., Bussemaker, H. J., Li, L., Sawado, T., et al. (2003).
881 Genomic binding by the Drosophila Myc, Max, Mad/Mnt transcription factor network. *Genes
882 & Development*, 17(9), 1101–1114. <http://doi.org/10.1101/gad.1066903>
- 883 Park, M., Patel, N., Keung, A. J., & Khalil, A. S. (2018). Engineering Epigenetic Regulation Using
884 Synthetic Read-Write Modules. *Cell*, 1–33. <http://doi.org/10.1016/j.cell.2018.11.002>
- 885 Patro, R., Duggal, G., Love, M. I., Irizarry, R. A., & Kingsford, C. (2017). Salmon provides fast
886 and bias-aware quantification of transcript expression. *Nature Methods*, 14(4), 417–419.
887 <http://doi.org/10.1038/nmeth.4197>
- 888 Pickersgill, H., Kalverda, B., de Wit, E., Talhout, W., Fornerod, M., & van Steensel, B. (2006).
889 Characterization of the Drosophila melanogaster genome at the nuclear lamina. *Nature
890 Genetics*, 38(9), 1005–1014. <http://doi.org/10.1038/ng1852>
- 891 Quinlan, A. R. A., & Hall, I. M. I. (2010). BEDTools: a flexible suite of utilities for comparing
892 genomic features. *Bioinformatics (Oxford, England)*, 26(6), 841–842.
893 <http://doi.org/10.1093/bioinformatics/btq033>
- 894 Ritchie, M. E., Phipson, B., Wu, D., Hu, Y., Law, C. W., Shi, W., & Smyth, G. K. (2015). limma
895 powers differential expression analyses for RNA-sequencing and microarray studies. *Nucleic
896 Acids Research*, 43(7), e47–e47. <http://doi.org/10.1093/nar/gkv007>
- 897 Rooijers, K., Markodimitraki, C. M., Rang, F. J., de Vries, S. S., Chialastri, A., de Luca, K. L., et
898 al. (2019). Simultaneous quantification of protein–DNA contacts and transcriptomes in single
899 cells. *Nature Biotechnology*. <https://doi.org/10.1038/s41587-019-0150-y>

- 900 Rotem, A., Ram, O., Shores, N., Sperling, R. A., Goren, A., Weitz, D. A., & Bernstein, B. E.
901 (2015). Single-cell ChIP-seq reveals cell subpopulations defined by chromatin state. *Nature*
902 *Biotechnology*, 33(11), 1165–U91. <http://doi.org/10.1038/nbt.3383>
- 903 Shen, J., Jiang, D., Fu, Y., Wu, X., Guo, H., Feng, B., et al. (2015). H3K4me3 epigenomic
904 landscape derived from ChIP-Seq of 1 000 mouse early embryonic cells. *Cell Research*, 25(1),
905 143–147. <http://doi.org/10.1038/cr.2014.119>
- 906 Singh, J., & Klar, A. (1992). Active genes in budding yeast display enhanced in vivo accessibility
907 to foreign dna methylases - a novel in vivo probe for chromatin structure of yeast. *Genes &*
908 *Development*, 6(2), 186–196. <http://doi.org/10.1101/gad.6.2.186>
- 909 Skene, P. J., Henikoff, J. G., & Henikoff, S. (2018). Targeted in situ genome-wide profiling with
910 high efficiency for low cell numbers. *Nature Protocols*, 13(5), 1006–1019.
911 <http://doi.org/10.1038/nprot.2018.015>
- 912 Southall, T. D., Gold, K. S., Egger, B., Davidson, C. M., Caygill, E. E., Marshall, O. J., & Brand,
913 A. H. (2013). Cell-Type-Specific Profiling of Gene Expression and Chromatin Binding without
914 Cell Isolation: Assaying RNA Pol II Occupancy in Neural Stem Cells, 26(1), 101–112.
915 <http://doi.org/10.1016/j.devcel.2013.05.020>
- 916 Unger, M. A., Chou, H. P., Thorsen, T., Scherer, A., & Quake, S. R. (2000). Monolithic
917 microfabricated valves and pumps by multilayer soft lithography. *Science (New York, NY)*,
918 288(5463), 113–116. <https://doi.org/10.1126/science.288.5463.113>
- 919 van Steensel, B., & Henikoff, S. (2000). Identification of in vivo DNA targets of chromatin
920 proteins using tethered dam methyltransferase. *Nature Biotechnology*, 18(4), 424–428.
921 <http://doi.org/10.1038/74487>
- 922 van Steensel, B., & Belmont, A. S. (2017). Lamina-Associated Domains: Links with Chromosome
923 Architecture, Heterochromatin, and Gene Repression. *Cell*, 169(5), 780–791.
924 <http://doi.org/10.1016/j.cell.2017.04.022>
- 925 Vogel, M. J., Peric-Hupkes, D., & van Steensel, B. (2007). Detection of in vivo protein–DNA
926 interactions using DamID in mammalian cells. *Nature Protocols*, 2(6), 1467–1478.
927 <http://doi.org/10.1038/nprot.2007.148>
- 928 White, J. A., & Streets, A. M. (2018). Controller for microfluidic large-scale integration.
929 *HardwareX*, 3, 135–145. <http://doi.org/10.1016/j.ohx.2017.10.002>
- 930 Wu, A. R., Kawahara, T. L. A., Rapticavoli, N. A., van Riggelen, J., Shroff, E. H., Xu, L., et al.
931 (2012). High throughput automated chromatin immunoprecipitation as a platform for drug
932 screening and antibody validation. *Lab on a Chip*, 12(12), 2190–2198.
933 <http://doi.org/10.1039/c2lc21290k>
- 934 Wu, F., Olson, B.G., & Yao, G. (2016). DamID-seq: Genome-wide Mapping of Protein-DNA
935 Interactions by High Throughput Sequencing of Adenine-methylated DNA Fragments. *JoVE*
936 (*Journal of Visualized Experiments*), (107), e53620–e53620. <http://doi.org/10.3791/53620>
- 937 Zhang, B., Zheng, H., Huang, B., Li, W., Xiang, Y., Peng, X., et al. (2016). Allelic reprogramming
938 of the histone modification H3K4me3 in early mammalian development. *Nature*, 537(7621),
939 553–557. <http://doi.org/10.1038/nature19361>
- 940
941
942
943

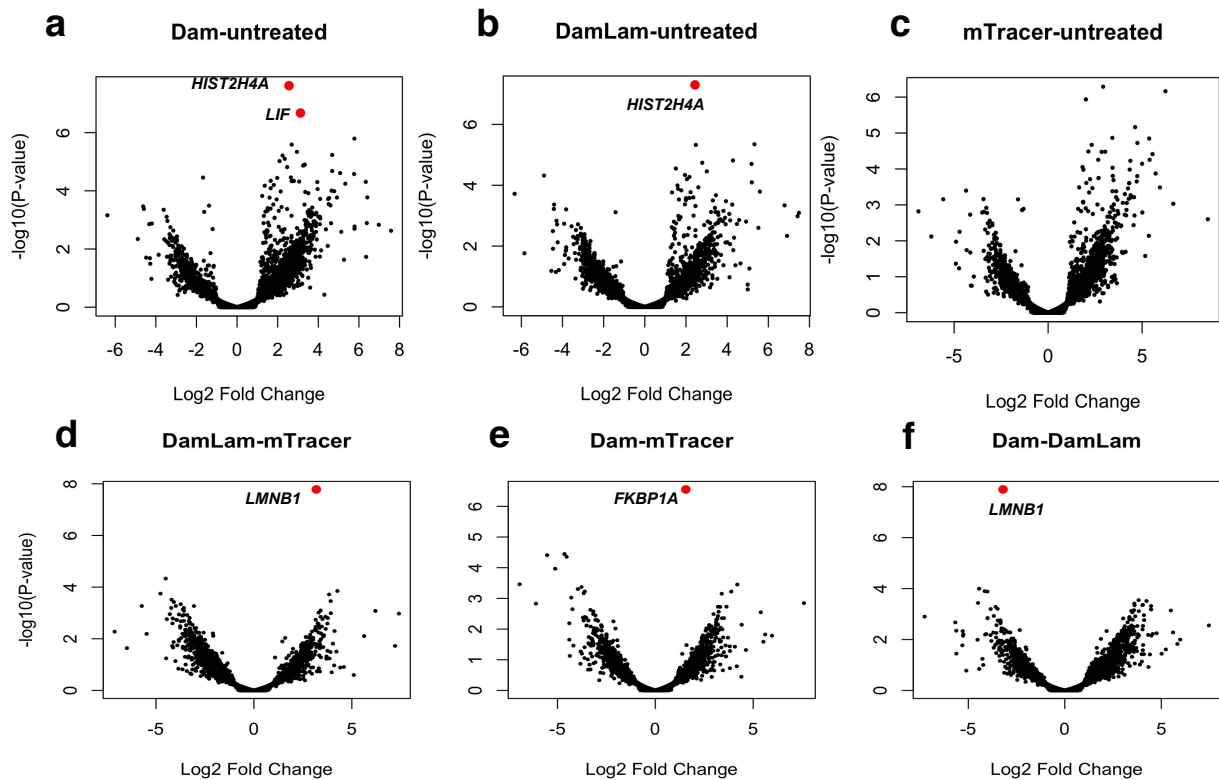
Supplementary Figures



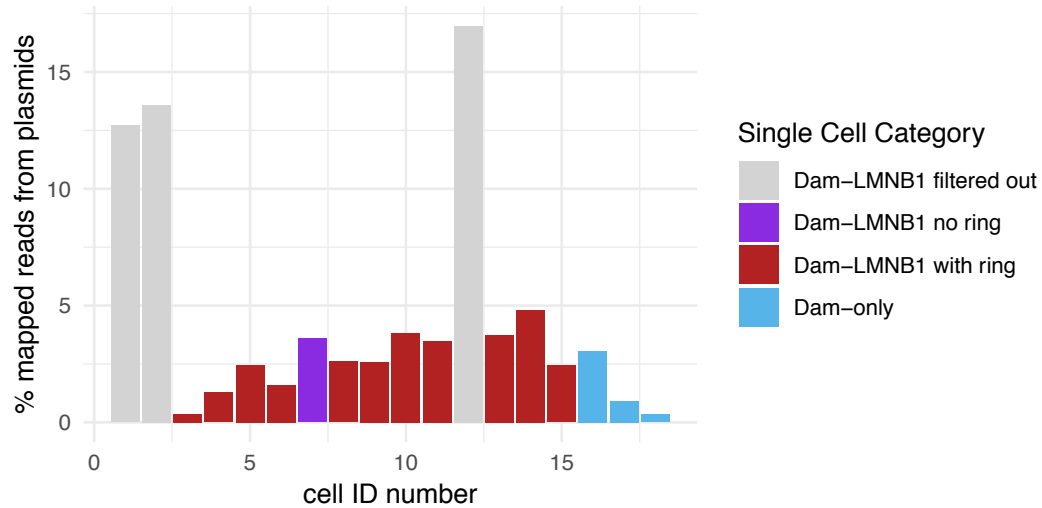
Supplementary Figure 1. Illustration of cell trapping procedure. Cells are driven through the device by peristaltic pumping or pressure-driven flow. Valves are actuated to confine the cell in the trapping region, where it is imaged, and if selected, is pushed by dead-end filling into a holding chamber to the right of the trapping region.



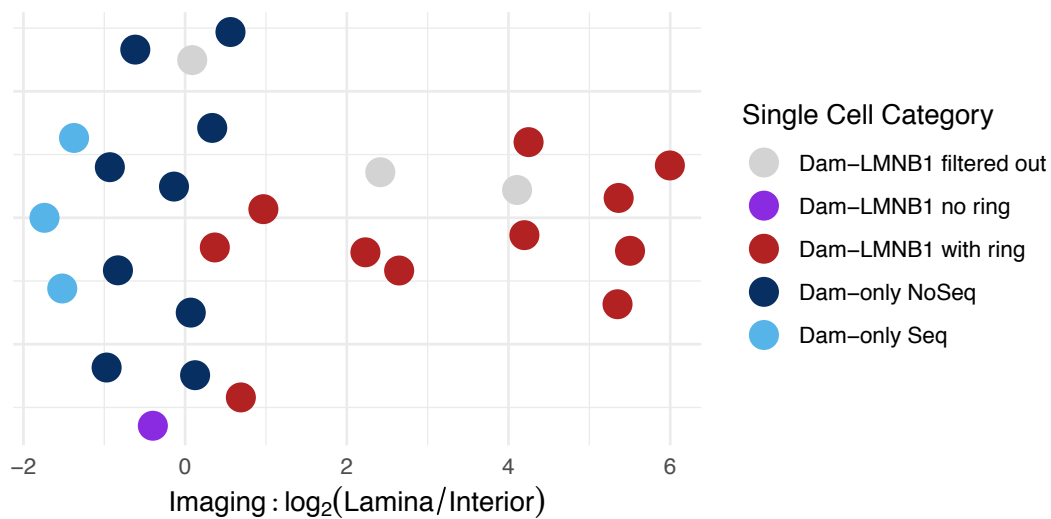
Supplementary Figure 2. Comparison of wild-type and V133A Dam alleles. (a) Kernel density estimate of log₂FoldChange from DESeq2 differential enrichment analysis of Dam-LMN1 coverage compared to Dam-only as reference. With V133A, more extreme log₂FoldChange values are observed with greater separation between the positive and negative log₂FoldChange peaks. In other words, compared to wild-type, the V133A Dam-LMN1 and Dam-only signals are more distinct. (b) Kernel density estimate of log₂ Fold Change, with cLAD/ciLAD classification from Lenain et al. 2017 indicated, shows greater separation for cLAD and ciLAD signal with V133A. (c) V133A has higher sensitivity than WT, with more differentially enriched regions at each log₂FoldChange threshold for calling significant differential enrichment.



Supplementary Figure 3. Volcano plots from differential gene expression analysis for RNA from bulk HEK293T cells transfected with Dam, *Dam-LMNB1*, ^{m6}A-Tracer, or no treatment control. Significantly differentially expressed genes (logFC significantly > 1 and adjusted p-value < 0.01) are indicated in red. Differentially expressed genes compared to no treatment control are *HIST2H4A* and *LIF* for Dam, *HIST2H4A* for Dam-LMNB1, and no genes for ^{m6}A-Tracer. When comparing Dam to ^{m6}A-Tracer, the only differentially expressed gene is *FKBP1A*, which is expected given the mutated FKBP1A-derived destabilization domain tethered to Dam in our construct. When comparing Dam-LMNB1 to ^{m6}A-Tracer, the only differentially expressed gene is *LMNB1*, which is again expected given *LMNB1* is expressed from the *Dam-LMNB1* construct itself.



Supplementary Figure 4. Percentage of mapped sequencing reads mapping to plasmid sequences for each single cell. Cells 1, 2, and 12 were filtered out due to their high plasmid DNA content.



Supplementary Figure 5. Lamina:Interior mean pixel intensity ratios for all cells. Imaging ratios are reported for each cell as in Figure 4d. Dark blue points represent Dam-only cells that were imaged by confocal microscopy but not sequenced, compared to the light blue points representing the Dam-only cells that were imaged by widefield microscopy and sequenced.